Chapter 4
Role of Doped Semiconductors in the Catalytic Activity

Ashish Gaurav, Ananta Paul, and Sushma Dave

Abstract There are several substances in today's world that are neither good conductors (metals) nor insulators (glass). At normal temperature, semiconductors are described as materials with a crystalline structure and very few free electrons. Examples of semiconductor include Silicon, carbon, germanium etc. At room temperature, the semiconductors act like an insulator with its resistivity which lies between that of conductor and insulator and most importantly, the conductivity can be controlled by addition of various impurities. Mostly, the semiconducting materials are crystalline in nature with rarely found semiconductor in form of amorphous and liquid. The electronic industries across the globe includes transistors, solar cells, light-emitting diodes (LEDs), and digital and analog integrated circuits are dependent on semiconductor technology. The diverse property of the semiconductor materials lies at the quantum level which includes the motions of the building blocks like electrons and holes in the crystal and lattice. Electrical conductivity being opposite to that of a metal and its conductivity can be tailored by adding impurities commonly known as doping or by applying different mechanism like electrical fields or lights. Conductivities in semiconductors are due to movement of free electron (n-type) and holes (p-type) and are sensitive to temperature, illumination, magnetic field and impurity atoms introduced. Controlling the concentration and location of p- and n-type dopant under a precise condition is utmost important for electronic devices.

A. Gaurav (✉)
Graduate Institute of Photonics and Optoelectronics, College of Electrical Engineering and Computer Science, National Taiwan University, Taipei City, Taiwan
e-mail: itsgaurav.bitm@gmail.com

A. Paul
Department of MEMS, IIT Mumbai, Mumbai, India

S. Dave
Department of Chemistry, JIET, Jodhpur, Rajasthan, India

S. Dave and J. Das (eds.), *Trends and Contemporary Technologies for Photocatalytic Degradation of Dyes*, Environmental Science and Engineering,
https://doi.org/10.1007/978-3-031-08991-6_4

4.1 Introduction

Nowadays semiconductor materials are used in every sector of modern technology. In technical purpose the high temperature materials are widely used (Rahman 2014).

Once compared to organic dyes and fluorescent proteins, semiconductor nanocrystals have unique physical and photoelectrical properties, such as high emission quantum yields, a narrow and symmetric emission peak with a broad excited wavelength, size-controlled fluorescence properties, and high optical stabilities (Khlyustova et al. 2020; Ilkme and Soylu 2021). But with the development of semiconductor nanocrystals, there is existence of many problems and challenges. In recent years, researchers found that doping impurities into these semiconductor materials could impact the various electrical, optical, and magnetic properties of the materials (Khlyustova et al. 2020; Yang and Lee 2017). So, intense studies have been going around the globe on impurity atoms such as Mn, Cu, Co, and many more doped semiconductor materials for their new enhanced properties and its application in various fields. Numerous techniques have been adopted till date to synthesize high quality doped semiconductor nanocrystals. Basically, doped semiconductor nanocrystals are usually synthesized by forming particular molecular precursors containing the specific constituent elements.

The introduction of impurities or defects into semiconductor lattices is a key method for influencing electrical conductivity, and it can also have a significant impact on the semiconductor's optical, luminescent, magnetic, and other physical properties. For example, whereas pure stoichiometric ZnO is an insulator, the conductivity of ZnO can be increased by a factor of ten with just minor changes in defect concentrations such as interstitial zinc or aluminium addition. Magnetic ions are one of the most intriguing types of dopants in semiconductors. Semiconductors with magnetic impurities, also known as diluted magnetic semiconductors or semimagnetic semiconductors, have been explored for decades (Lee et al. 2018; Zhang et al. 2019). "Giant Zeeman effects" observed in the excitonic levels drew the attention and toward diluted magnetic semiconductors (Li et al. 2021, p. 4; Chen and Pan 2021). The excitonic Zeeman parting of DMSs regularly surpass the parting of the relating nonmagnetic semiconductors by more than two significant degrees, leading to potential applications in optical gating (Ambigadevi et al. 2020). All the more as of late, consideration in DMSs has moved to their utilization in spintronics, or turn based hardware advances (Chen et al. 2020; González-Rodríguez et al. 2020). The gigantic Zeeman parting is used to make turn settled conductivity directs in semiconductors in this field. The subsequent twist energized flows might give different take based on levels of opportunity to semiconductor gadgets, possibly expanding the data content of a charge beat and presenting new capacities not found in current-based semiconductors. Nanoscale DMSs have been utilized as major functional parts in a large number of the gadgets proposed by theoreticians or tried in model forms by experimentalists (Bi et al. 2020; Fu et al. 2020; Sheng et al. 2020). Luminescence Glow activators are one more significant class of dopants for semiconductor nanocrystals. For as long as decade, a large part of the examination into unadulterated

semiconductor nanocrystals has been driven by interest in their glowing properties, and controlling these nanocrystals' properties by doping with particles like Mn_2 or Eu_2 can possibly widen the scope of valuable spectroscopic properties that can be accomplished from this class of materials. These glowing luminous colloids are alluring possibilities for optical imaging applications in light of their high quantum yields, slight discharge line morphologies, and expansive excitation profiles. Electronic dopants, what work as shallow donors or acceptors inside the semiconductor band structure to present transporters, are a third intriguing gathering of dopants (Shah et al. 2021; Dave et al. 2021a). Although electronic doping of nanocrystals has not yet been extensively investigated, it is evident that as self-assembled device structures become more accessible, this field will play a significant role in the future of nanotechnology (Bryan and Gamelin 2005). As a result of the exponential expansion in industrialization, both energy and environmental challenges have arisen. The primary source of energy is fossil fuels, such as coal, oil, and natural gas. Fossil fuels, which are used as a primary source of energy, are also responsible for many types of environmental pollution, as air and water pollution have expanded dramatically in recent years, affecting a vast number of cultures around the world (Zhao et al. 2019). In 1972, Fujishima and Honda first founded that the TiO_2 electrode can break down hydrogen in aquatic production under ultraviolet light (UV) (Zhang et al. 2019). Since then, photocatalysis activities have attracted intense attention and researcher from across the globe due to its several advantages such as low cost and attractive efficiency with feature of direct conversion of solar energy to easily stored hydrogen, with no harm to environment as it is a unique process for rectifying energy and environmental issues like degradation of various organic pollutants in wastewater, production of hydrogen, purification of air, and antibacterial activity (Bao et al. 2008). Photocatalysis is a combination of photochemistry and catalysis in which light and catalysts are employed in tandem to speed up chemical reactions. Photocatalysis is defined as "catalysis-driven acceleration of a light-induced process" in simple terms. Photocatalysts are classified as either homogeneous or heterogeneous processes. Furthermore, Frank and Bard successfully oxidized CN- to OCN- using TiO_2 as a photocatalyst, an experiment that offered optimism for the use of photocatalysts in wastewater treatment (Tong et al. 2012). Since then, TiO_2 has been widely accepted as a photocatalyst for a wide range of applications in the field of environmental management. The broader research area currently at this stage includes photocatalyst disinfection (Guha et al. 2003, p. 2), photocatalytic hydrogen production (You et al. 2010; Giahi et al. 2019), photocatalytic reduction of CO_2 (Rahman et al. 2021; Moballegh et al. 2007), photocatalyst wastewater treatment (Szabó-Bárdos et al. 2003; Goto et al. 2004; Li et al. 2004; Kwon et al. 2000), and air purification (Subramanian et al. 2003). Xing et al. (2006) presented the application of photocatalysts in air treatment, including catalyst development and reactor design. Masakazu and Takahit (1987) gave an update on photocatalytic sterilization's recent developments and problems. The majority of existing reviews concentrate on only one or a few characteristics of photocatalysts (Zhang et al. 2019).

4.2 Photocatalytic Mechanism and Influencing Factor

4.2.1 Reaction Mechanism

Photocatalytic response is a synthetic cycle that happens under the coupled activities of light and the photo impetus with different benefits like protection of environment and remarkable toxin destruction with no supplementary products. The fundamental component of a photocatalytic response is portrayed in Fig. 4.1. Photocatalytic activity is characterized as the light-prompted redox response of semiconductors from the point of view of semiconductor photochemistry. Because of their discrete electronic states, semiconducting materials are ordinarily utilized as an impetus that can go about as a sensitizer for the illumination of light reforming redox processes. A semiconductor structure has an energy band structure that comprises of a low-energy valence band (VB) and a high-energy conduction band (CB), with a prohibited band between the conduction and valence groups. At the point when the occurrence light's energy is more noteworthy than the semiconductor's band hole, the electrons in the VB of the semiconductor are unsettled and travel toward the conduction band, making openings structure in the VB. Photogenerated electrons and openings are isolated by an electric field and move to the outer layer of semiconductor particles (Satapathy et al. 2021; Dave et al. 2021c).

Photogenerated pores have huge oxidizing qualities and can oxidize atoms adsorbed on the semiconductor's surface or in its answer. The itemized course of a photocatalytic response is as per the following. Under a specific energy of light,

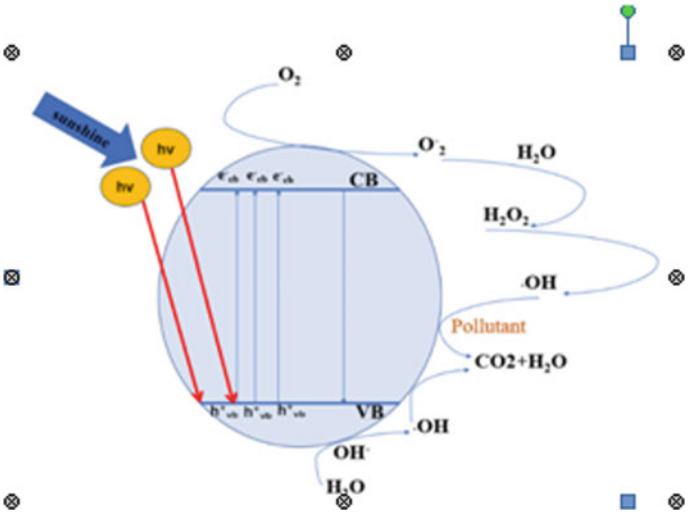

Fig. 4.1 Principle mechanism of a photocatalytic reaction [Reproduced from Zhang et al. (2019) open access]

electrons on a VB are invigorated and leap to a CB, and the openings stay on the VB. The openings on the VB diffuse to the photocatalyst surface and participate in an oxidation interaction, while the electrons on the CB travel to the impetus surface and partake in a decrease response. The electrons can make H_2O_2 or a superoxide revolutionary O_2-with H+ and disintegrated O_2 in the fluid arrangement during the interaction, and the openings can oxidize OH– to create hydroxyl extremists OH, bringing about the degradation of pollutants (Santra and Kamat 2012; Li et al. 2014; Ertis and Boz 2017; Ranjith et al. 2018).

Many factors influence photocatalytic activity, including the catalyst and its properties, surface conditions (charge, adsorbed materials, defect, and composition), reaction media (pH, solvent), light source, and varied reactant concentrations, adsorption, and so on (Dave et al. 2021b).

4.3 Metal-Doped Semiconductor

4.3.1 Silver and Gold Doped Semiconductor

4.3.1.1 Effect of Doping on XRD Pattern

To modify the photocatalytic activity of different semiconductors (TiO_2, ZnO, and CdS), various metal ions (Au, Ag, Pt, and Pd) are doped in the semiconductor materials. Doping with two atoms (co-doping) into semiconductors also has a significant interest for a superior photocatalytic activity.

Figure 4.2 has shown the XRD characterization and pattern of precipitation-decomposition method, Ag doped Au–ZnO shows that it has both hexagonal and wurtzite structure (Senthilraja et al. 2014).

For the bare ZnO all the diffraction peaks matched with standard JCPDS 89-0511. It was found that with the incorporation of 3% Ag, the crystallite size of bare ZnO and co-doped Ag–Au–ZnO semiconductor are found to be almost equal to 4.15 and 4.14 respectively. The crystallite size was determined by the Debye-Scherrer equation given by:

$$D = \frac{K\lambda}{\beta \cos\theta}$$

where D is the crystal size, K is the dimensionless constant, λ is the wavelength of X-ray, β is the full width at half-maximum of the diffraction peak and θ is the diffraction angle.

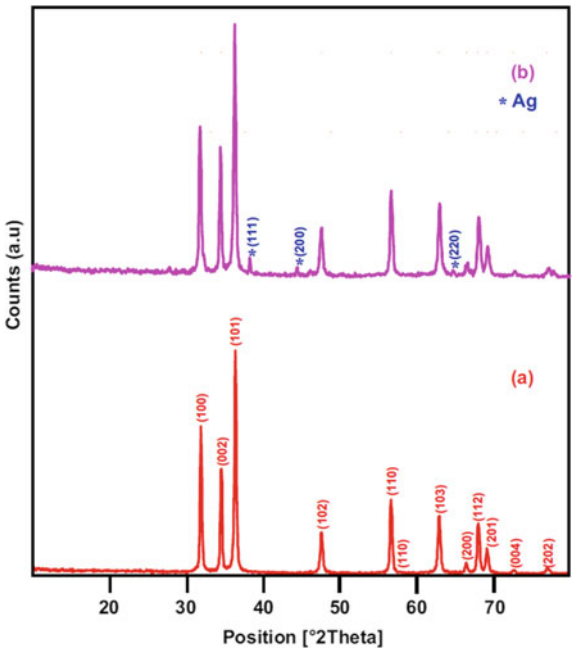

Fig. 4.2 XRD patterns of **a** bare ZnO and **b** Ag–Au–ZnO [Reproduced with permissions from Senthilraja et al. (2014)]

4.3.1.2 Effect of Doping on Morphology

The photocatalytic activity of the crystal is influenced by the structure and morphology of the catalyst. The FESEM image were used to examine the surface morphology of Ag–Au–ZnO. Figure 4.3 shows that the particles are both spherical and hexagonal in shape.

The particle size varies from 4 to 100 nm and these changes of the morphology increase the photocatalytic activity of Ag–Au–ZnO.

4.3.1.3 Effect of Doping on Surface Area

The most critical element influencing photocatalytic activity is the surface area of the catalyst. The surface area was measured by nitrogen gas absorption method. The surface area of Ag–Au–ZnO (20.3 m^2g^{-1}) is higher compared to bare ZnO (14.9 m^2g^{-1}). The increased surface area increases the number of active sites on the surface of the catalyst, resulting in increased photocatalytic activity. The single point total pore volume also increased for Ag–Au–ZnO as per the results.

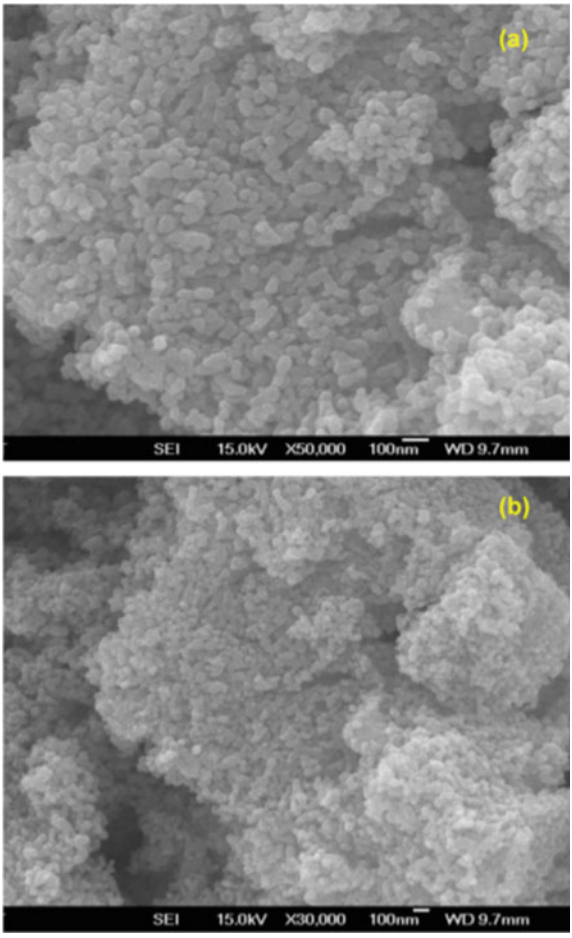

Fig. 4.3 FE-SEM images of **a** Ag–Au–ZnO (100 nm) and **b** Ag–Au–ZnO (100 nm) [Reproduced with permissions from Senthilraja et al. (2014)]

4.3.2 Silver Doped Semiconductor

4.3.2.1 Effect of Doping on XRD

The XRD pattern of Ag doped ZnO shown in Fig. 4.4 exhibits a minor change in intensity of the (101) plane but preserved the wurtzite ZnO structure. The change in the intensity was associated to the changes in the grain size (Vallejo et al. 2020).

4.3.2.2 Effect of Doping on Morphology

The effect of Ag doped ZnO was shown in the morphology. The roughness and grain size of the pristine ZnO and Ag–ZnO varies from 18.4 nm to 36.6 nm and 190 nm to

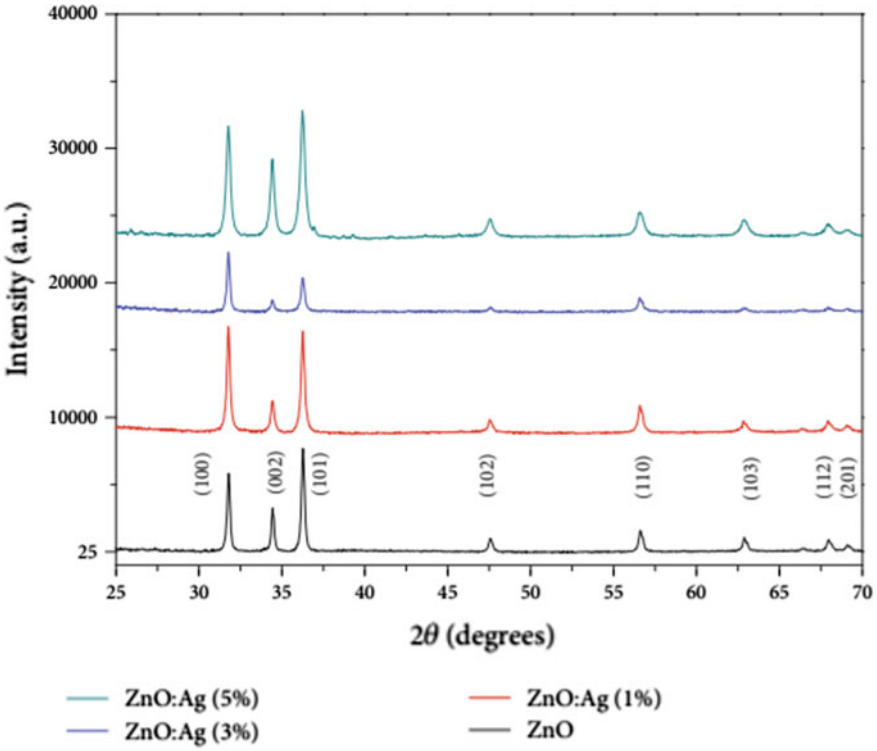

Fig. 4.4 X-ray diffraction patterns for both ZnO and ZnO: Ag thin films [Reproduced with permissions from Vallejo et al. (2020)]

120 nm respectively. The decrease in the grain size is attributed to the incorporation of Ag in the ZnO lattice.

4.3.2.3 Effect of Doping on Optical Properties

The effect of Ag doped ZnO was also realized in optical properties. For pure ZnO, the reflectance was very high (70%) after 350 nm. Figure 4.5 shows that with incorporation of Ag the reflectance spectrum decreases continuously in the visible range. It was also observed that due to oxygen vacancy in the ZnO structure, the bandgap of doped semiconductor decreased from 3.22 eV (ZnO) to 3.10 eV (5% Ag–ZnO) with increasing Ag concentration. Oxygen vacancies are the most favorable defects procedure during ZnO synthesis.

The bandgap E_g of all the samples determined using the Kubelka–Munk function and tauc plot is calculated using following equations:

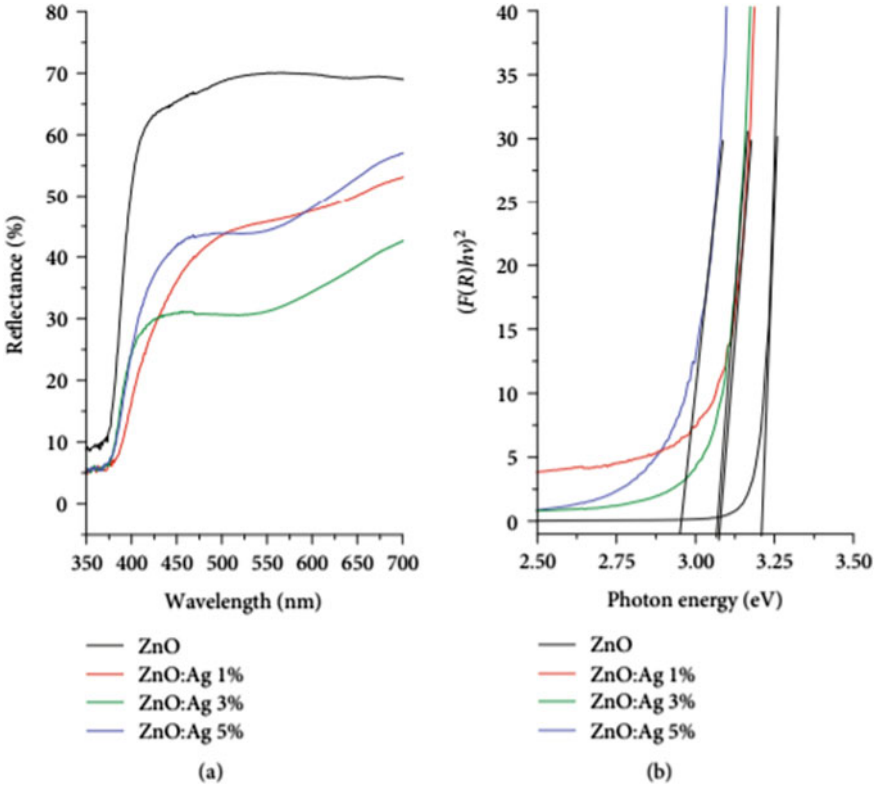

Fig. 4.5 **a** Reflectance diffuse spectra for both ZnO and ZnO:Ag thin films. **b** Kubelka–Munk plots and band gap energy estimation for both ZnO and ZnO:Ag thin films [Reproduced with permissions from Vallejo et al. (2020)]

$$F(R_\infty) = \frac{(1 - R_\infty)^2}{2R_\infty}$$

$$(F(R_\infty)h\upsilon)^{1/2} = A\left(h\upsilon - E_g\right)$$

where $F(R_\infty)$ proportional to the absorption coefficient, λ is the wavelength, E_g is the bandgap, A is the constant.

4.3.2.4 Effect of Doping on Photocatalysis

The Ag doped ZnO exhibit better photocatalytic performance compared to the pure ZnO. With Ag doping, the photocatalytic performance was enhanced because of the reduction in grain size and intra-band transition. The photo degradation performance also increased by 16.5 times with 5% Ag doping.

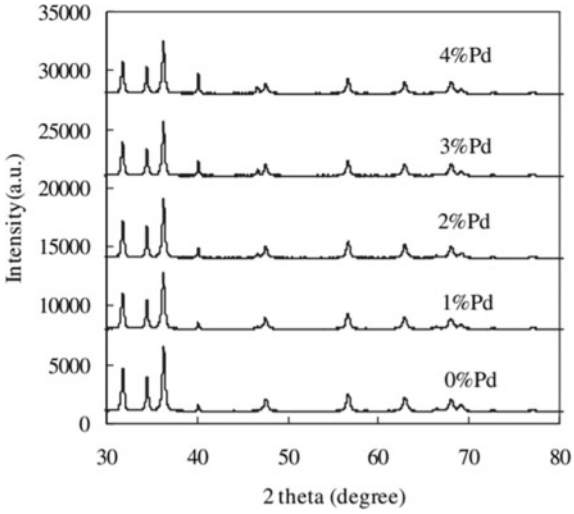

Fig. 4.6 XRD patterns of photocatalysts [Reproduced with permissions from Zhong et al. (2012)]

4.3.3 Palladium Doped Semiconductor

4.3.3.1 Effect of Doping on XRD Patterns

The XRD pattern of Pd doped ZnO (Fig. 4.6) shows that it exhibits both hexagonal wurtzite structure. For the bare ZnO, all the diffraction peaks matched with standard JCPDS 89-0511. There are no traces of PdO which depicts that Pd enters the ZnO lattice.

The crystallite size was determined by the Debye–Scherrer equation and it was observed that the crystallite size increased from 25 to 33 nm with increased Pd concentrations (Zhong et al. 2012).

4.3.3.2 Effect of Doping on Optical Properties

The effect of Pd doped ZnO was also shown in optical properties. For pure ZnO, the reflectance was very high after 350 nm but with incorporation Pd concentration the reflectance decreases continuously as shown in Fig. 4.7.

Pd doped ZnO samples shows higher absorption in the visible range which indicates that with incorporation of Pd in ZnO crystal there might be some trapping states formed (inter-band trap site). By absorbing visible light electrons are excited from valance band of ZnO and captured by the inter-band trap sites. The absorption of the electron by the trap states can promote the photocatalytic activity of the doped samples.

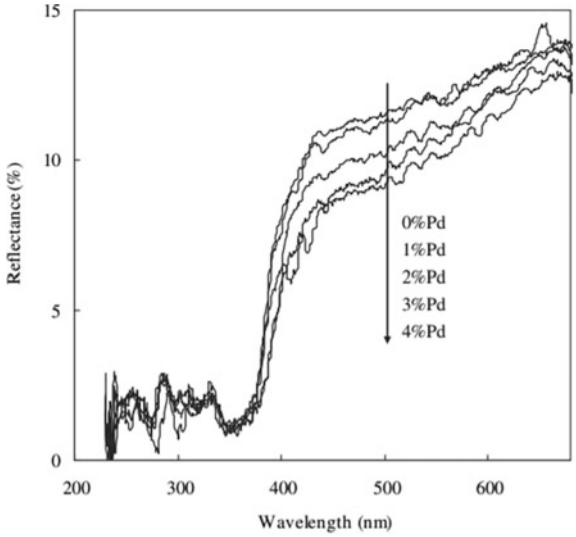

Fig. 4.7 UV/vis diffuse reflectance spectra of photocatalysts [Reproduced with permissions from Zhong et al. (2012)]

4.3.3.3 Effect of Doping on Surface Area

The surface area is measured by nitrogen gas absorption method. The surface area of ZnO (7.24 m^2g^{-1}) is higher compared to Pd doped ZnO (6.49 m^2g^{-1}) (4%). The decreased surface area of the doped samples is due to the larger crystal size of Pd–ZnO. The single point total pore volume also decreased for Pd–ZnO.

4.3.3.4 Photocatalytic Activity

A better performance is seen in the photo catalytic activity of the Pd doped samples in comparison to pure ZnO. The photocatalysis degradation of ZnO occurs due to the generation of an electron-holepair and various radicals such as hydroxyl (•OH), hydroperoxyl (•OOH) and superoxide (O_2•–) radicals. Out of these radicals, hydroxyl (•OH) radical known as most powerful oxidizing species which can attack the organic pollutant near to the surface of the photocatalyst. The ZnO crystal enhanced by Pd doping which was observed that for 3% of Pd doping shows higher photocatalytic activity. The improved photocatalytic activity with doped ZnO is due to increased absorption capability of light and the separation rate of photo induced charge carriers.

In todays' world, a diverse amount of research is going on in the field of doped semiconductors and its role in catalytic activities. Some of the most common doped semiconductor reported includes Ag, Au and Pt/Pd doping and its characteristics effect in the field of catalytic properties and applications. In this book chapter we are going to focus on the some of the doped semiconductor and its significant application and role in catalytic activities.

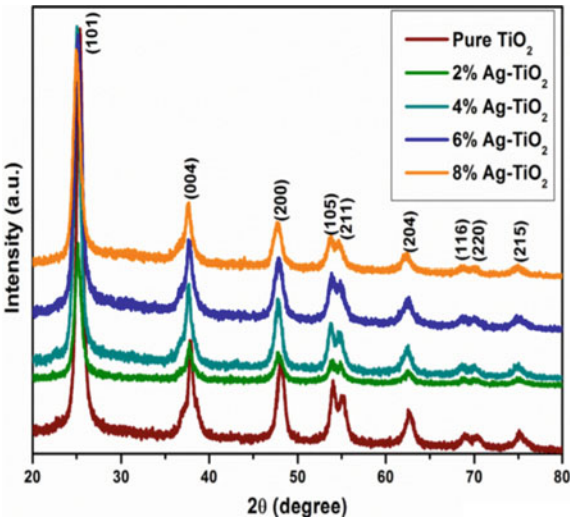

Fig. 4.8 The XRD patterns of the pure and Ag-doped TiO_2 NPs [Reproduced with permissions from Ali et al. (2018)]

4.3.4 Ag-Doped TiO_2

4.3.4.1 XRD Analysis

To explore the crystal structure of pure and Ag–TiO_2 NPs calcined at 400 °C, XRD analysis was carried out in the range of 20°–80°. Figure 4.8 is showing the diffraction peaks in correspondence to the anatase phase of TiO_2 (JCPSD Card: 21e1272).

It emphasizes that Ag doping concentration has no effect on the anatase phase. Furthermore, the absence of an impurity phase demonstrated the successful incorporation of silver ion into the TiO_2 matrix structure. However, as doping ion concentration increases, the primary diffraction peak changes towards the lower 2 value and broadens, which could be attributed to lattice strain in the materials. Using the Williamson Hall relation, the average crystallite size (D) and lattice strain () may be calculated from the diffraction peaks' full-widths at half-maximum (FWHM) (Santra and Kamat 2012). XRD data are used to calculate the average crystallite size (D), lattice strain, lattice parameters (a, b, and c), and lattice volume for all samples. However, when the amount of Ag doped increases (from 0 to 2.0 mol percent), the lattice properties and average crystallite size drop (Ali et al. 2018).

4.3.4.2 Raman Analysis

The Raman peaks for pure TiO_2 and Ag-doped TiO_2 NPs showed (Fig. 4.9) a similar pattern to that of anatase TiO_2.

There is no trace of silver oxide peaks which explains that the Raman spectral results are good agreement with XRD observation. Moreover, Ag-doped TiO_2NPs

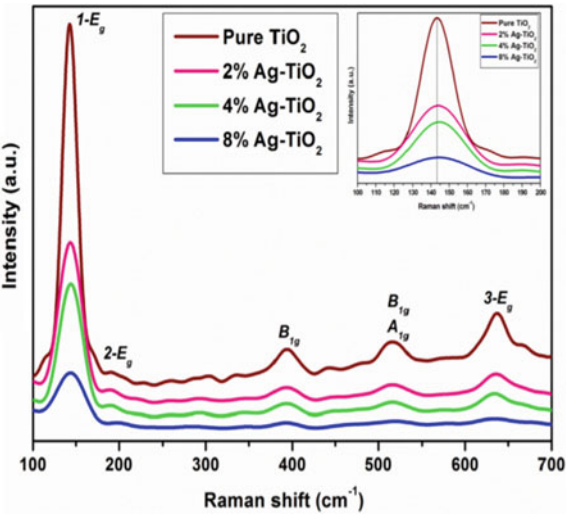

Fig. 4.9 Raman spectra of pure and Ag-doped TiO_2 NPs [Reproduced with permissions from Ali et al. (2018)]

conserved the anatase structure which suggests that Ag dopants are substitutional combined into the structure of TiO_2 framework.

4.3.4.3 Optical Properties

The effect of Ag doped TiO_2 was also shown in Fig. 4.10.

With increasing Ag concentration, it was shown that the bandgap of doped semiconductors drops from 3.12 (TiO_2) to 2.6 (8% Ag–TiO_2) due to oxygen vacancies in

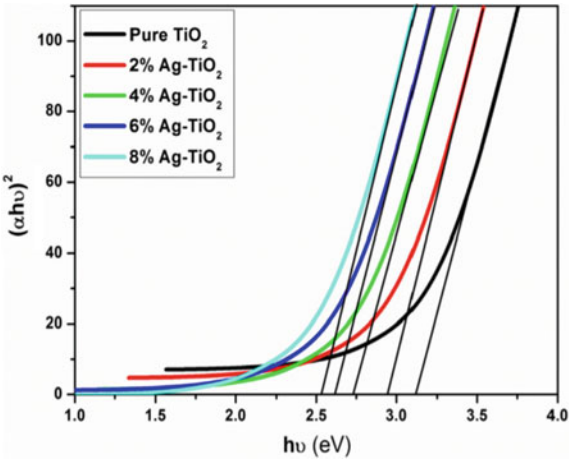

Fig. 4.10 Optical band gap energy plot of pure and Ag-doped TiO_2 NPs [Reproduced with permissions from Ali et al. (2018)]

the TiO_2 structure. During ZnO production, oxygen vacancies are the most desirable flaws.

4.3.4.4 Photocatalytic Properties

The photocatalytic activity of pure and Ag-doped TiO_2 photo-catalysts was tested using methylene blue dye photodegradation. The results showed that when exposed to visible light, an Ag-doped TiO_2 photocatalyst can efficiently degrade MB, with 4.0 mol percent Ag-doped TiO_2 having the highest photocatalytic activity of all the sol-gel samples.

4.3.5 Au–TiO_2

4.3.5.1 Experiment

Using 150 mL of hydrochloric acid, 0.75 g of pristine single-walled carbon nanotubes (SWCNT) (quality 98%; D2-10 nm; L 0.3–3 μm) were chemically activated, resulting in the production of oxygen groups on the SWCNT surface. The mixture was ultrasonically sonicated for 10 min at 40 °C, then poured with deionized water, filtered under vacuum, and dried for 12 h at 120 °C. The tertiary TiO_2/Au/SWCNT nanocomposites were made using the sol-gel technique. To begin, 300 mg modified SWNT and 0.4 ml titanium isopropoxide (TTIP) were dissolved in 100 ml deionized water and agitated for 20 min at 30 °C. The pH range was preserved at 4 by adding 4 ml of 1 M nitric acid to the solution. 20 mg of gold chloride ($Au/TiO_2 = 10\%$) was dissolved in 100 ml of deionized water and heated to form the Au solution. Temperature of fusion after being added to an Au solution, the TiO_2 SWNT combination was agitated for two hours. After that, the temperature, coolant, and 20 mL of 0.01 M sodium citrate solution in water were added, and the mixture was continually stirred for another hour. The mixture was heated to 80 °C overnight before incubation at 500 °C for 3 h. To make a pure TiO_2 and TiO_2/Au binary nanocomposite, the same procedures were used without the use of SWCNT (Mohammed 2020).

4.3.5.2 XRD Data

The X-ray diffraction patterns of TiO_2/Au binary and TiO_2/Au/SWCNT ternary nanohybrids show a preference for orientation in the (101) direction at about 25.32° for the anatase phase of TiO_2, with low intense peaks located at 37.37°, 47.44°, 53.851°, and 55.1°, respectively, corresponding to (004), (200), (105), and (211) planes The major XRD peak of the Au is not highlighted due to the overlapping of Au (004) peak and titanium dioxide (111) peak (Fig. 4.11).

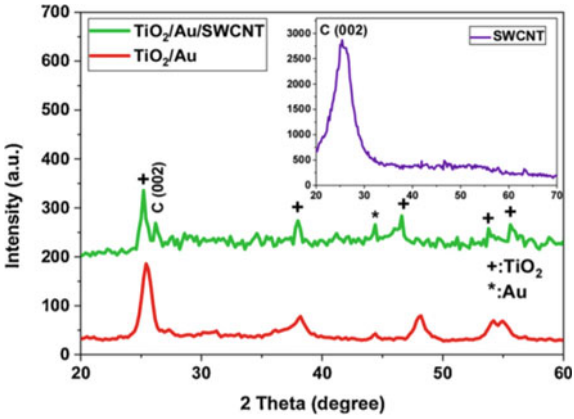

Fig. 4.11 XRD patterns of TiO_2/Au and TiO_2/Au/SWCNT nanohybrid. XRD pattern of raw SWCNT (inset) [Reproduced with permissions from Mohammed (2020)]

The XRD pattern of TiO_2/Au/SWCNT nanohybrid shows the SWCNT (002) diffraction peak at around 26.17°, this increasing in the angle position can be credited to the decrease of interplanar distance between carbon tubes after loading of TiO_2/Au nanoparticles. The intensity of all XRD peaks of the TiO_2/Au unit decreases with the addition of Au dopant and SWCNT because the crystal growth kinetics is affected by the chemical reactivity of the dopant. The particle size of TiO_2/Au and TiO_2/Au/SWCNT are 15 nm and 11 nm respectively.

4.3.5.3 FESEM Data

From the FESEM image (Fig. 4.12), it is clear that the SWCNTs have a tube-like structure with diverse outer diameters and tube lengths. By TiO_2/Au image, the small particles obviously own a spherical shape with different sizes (10–150 nm).

The FESEM image of the TiO_2/Au/SWCNT nanocomposite showed that the TiO_2/Au particles were anchored to the wall of the SWCNTs and the aggregation was also shown in a few locations.

4.3.5.4 Optical Properties

The Tauc relationship was used to determine the band gap of the tertiary hybrids TiO_2, TiO_2/Au, and TiO_2/Au/SWCNT using UV-vis spectra. The band gap of virgin TiO_2 is roughly 3.18 eV, which is similar to the normal band gap of bulk titanium oxide. When Au is included into TiO_2, however, the band gap decreases from 3.18 to 2.93 eV for TiO_2/Au and to 1.95 eV for TiO_2/Au/SWCNT.

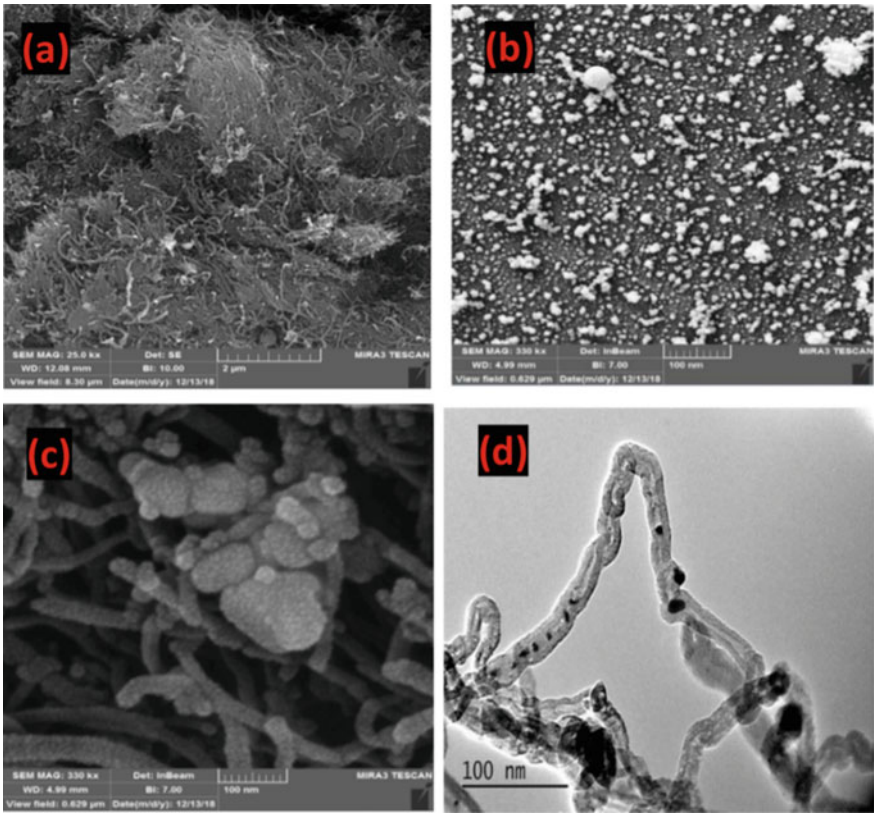

Fig. 4.12 FESEM images of **a** raw SWCNT, **b** TiO_2/Au, **c** TiO_2/Au/SWCNT, and **d** HRTEM of TiO_2/Au/SWCNT nanohybrid [Reproduced with permissions from Mohammed (2020)]

4.3.5.5 Photocatalytic Activity

Ternary nanohybrid estimation shows moderately uniform TiO_2/Au nanoparticles stacking in the SWCNT framework with upgraded UV-vis retention highlights. The TiO_2/Au/SWCNT showed higher effectiveness for the decolorization and mineralization of MB color under sunlight based reenacted light contrasted and unblemished TiO_2 and TiO_2/Au. Since the TiO_2/Au/SWCNT nanohybrids enormously dislodged light assimilation to a more extended frequency, lower energy was required for photocatalytic execution and the MB color corruption effectiveness developed. The current discoveries affirm that the improved photocatalytic action of TiO_2/Au/SWCNT by SWCNTs doing as an adsorbent, framework specialist and charge acceptor to catch photo created electrons from the TiO_2 conduction band because of apparent light illumination and henceforth forestalling the e– to h+ pair recombination.

4.3.5.6 Pt/Pd-TiO_2

The impregnation process was used to create the modified TiO_2. At 373 K, 600 mg TiO_2 (Degussa P25) was agitated in a succession of concentrations of $H_2PtCl_6$and $PdCl_2$ solutions for 60 min. The resulting Pt_4+/TiO_2 and Pd_2+/TiO_2 slurries were then vacuum freeze-dried for 20 h (100–200 mTorr at 57.5 °C). Pt-doped TiO_2 and Pd-doped TiO_2 samples were obtained in a tubular oven at progressively higher temperatures (30, 120, and 400 °C) for 3 h. Before further characterizations, the as-prepared Pt-doped TiO_2 and Pd-doped TiO_2 were exposed to air for 3 h, a period similar to that used in the kinetic studies. Pt-doped TiO_2 and Pd-doped TiO_2 reduced at 400 °C is abbreviated as Pt/TiO_2 and Pd/TiO_2, respectively, on the next pages.

4.3.5.7 Photocatalytic Applications

Photocatalysis is a versatile technique with a lot of room for growth. The applications of various semiconductor photocatalytic shown in Fig. 4.13.

Houas et al. (2001) used methylene blue to imitate environmental wastewater in 2001. The researchers discovered that photocatalysts based on titanium dioxide which could successfully decompose methylene blue. Lachheb et al. (2002) irradiated titanium dioxide photocatalyst with UV light to accomplish dye degradation (alizarin S, crocein orange G, methyl red, Congo red, and methylene blue). The experimental results revealed that the five dyes not only decolorized but also disintegrated completely. Liu et al. (2018) used a conventional electrospinning approach

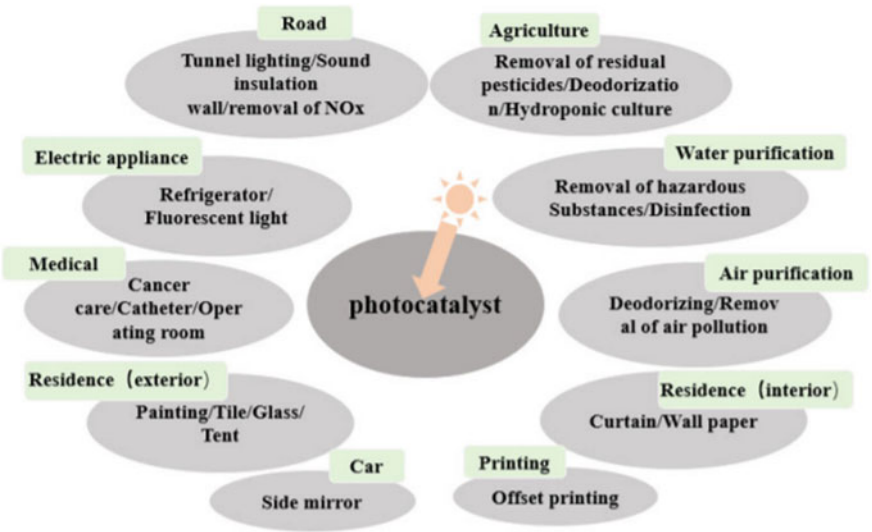

Fig. 4.13 Various applications of Semiconductor photocatalysis [Reproduced from Zhang et al. (2019) open access]

with a calcination procedure to create flexible composite Fe_2O_3/TiO_2 nanofibers, which they effectively used for photocatalytic wastewater treatment and photocurrent monitoring. Nigussie et al. (2018) reported Ag–TiO_2 and Ag–ZnO NPs with high thermal stability and strong antibacterial activity which is expected to serve in applications in the pharmaceutical and nanocomposite fields and also in antibacterial activities.

Demirci et al. (2016) showed that Ag-doped TiO_2 films had a better photocatalytic activity than undoped TiO_2 film. In comparison to undoped TiO_2 films, Ag replacement in TiO_2 matrix increased photocatalytic activity of TiO_2 films under UV light irradiation. This study revealed the effectiveness of using Ag-doped film to remove dissolved organic pollutants in water.

Guillén-Santiago et al. (2010) reported undoped and Ag-doped TiO_2 thin films onto glass substrates deposited by the sol-gel technique. The film thickness is controlled indirectly by the immersions number, and the aging time of the starting solution plays an important role in the degradation performance of MB. A 35% of MB degradation is reached using UV-irradiation. As a result, the photocatalysis processes showed that Ag-doped TiO_2 thin films are attractive for applications in water cleaning. Kumar et al. (2015) reported simple solution technique at low temperature which was employed to make Ag-doped ZnO nanoellipsoids, which were used as an effective photocatalyst and efficient electron mediator in the production of a highly sensitive and robust hydrazine chemical sensor.

Khurshid et al. (2019) have stated artificial hydrothermal method used for the fruitful preparation of ZnO: Ag/rGO nanocomposites. The photo-electrochemical properties of ZnO: Ag/rGO were methodically examined and results were linked with pristine ZnO. The results revealed that the ZnO: Ag/rGO nanocomposite can be employed as a good photoanode in electrochemical applications. According to Muoz-Fernandez et al. (2016), noble metal (Pt, Ag)/ZnO nanoparticles were successfully manufactured by a simple solvothermal process at low temperature and short reaction periods. In all of the photocatalytic studies, MB removal was greater than 70%, confirming the system's potential for wastewater treatment applications.

Ahmad reported et al. (2014) Mn–ZnO/Graphene nanocomposites photocatalysts synthesized via solvothermal method with good control of the coating density. It was found that all Mn–ZnO/Graphenenanocomposites had stronger light absorption in the visible light region than pure and doped ZnO. The 3% Mn–ZnO/Graphene photocatalyst showed superior photocatalytic activity than Mn–ZnO/Graphene, Mn–ZnO, and ZnO for the degradation of MB used as test pollutant under visible light irradiation. This study provides a new possibility in the investigation of ZnO/Graphene nanocomposites and its practical applications in the field of environmental science.

Till date, Molybdenum disulfide (MoS_2) nanosheets, because of exceptionally dynamic nature, and being efficient shows their promising application in the reactant decrease of nitroarenes.

Molybdenum disulfide (MoS_2) nanosheets doped with progress metal is a notable system embraced to upgrade their catalyst effectiveness for the decrease of nitroarenes, nonetheless, the specific and ideal measure of doping is as yet questionable and a subject of future research. Rahman et al. (2021) detailed the creation

of couple layered cobalt doped MoS_2 nanosheets with various cobalt content (2, 4, 6, and 8%) by means of the solvothermal technique with appropriate tuning of Co focus as doping in MoS_2 nanosheets with a point of finding a potential alternative of a respectable metal impetus for the reactant decrease of nitroarenes, utilizing sodium molybdate dihydrate ($Na_2MoO_4.2H_2O$), thiourea (CH_4N_2S) and cobalt acetate tetrahydrate [$Co(CH_3COO)_2.4H_2O$] as antecedents and their catalyst execution has been analyzed by monitoring the decrease of p-nitrophenol by NaBH4 continuously utilizing UV-apparent absorption spectroscopy. As per the result, the 6% Co doped MoS_2 nanosheets exhibited predominant reactant movement with a pseudo-first request rate steady of $3.03 \times 103\ s^{-1}$ corresponding to the bountiful deformities in the active edge destinations having a prevailing metallic 1T stage with Co particle initiated inadequate basal planes, sulfur (S) edges, catalytic primary and electronic tweak among MoS_2 and Co particles and enhanced electron move helped through redox cycling in the dynamic locales. The analysis performed showed that the undoped and unique (2, 4, 6, and 8%) nuclear weight rates of cobalt doped MoS_2 nanosheets with the cobalt particle actuated on faulty basal planes, S-edges, Mo locales were incorporated in a solitary advance aqueous response process. The viability of the pre-arranged MoS_2 nanostructures as impetuses for the decrease of 4-nitrophenol to 4-aminophenol in abundance $NaBH_4$ was additionally analyzed. It was found that different arranged morphologies of MoS_2 nanostructures were viewed as powerful and stable impetuses and followed pseudo-first-request energy. Moreover, the catalyst movement property was obviously seen to improve with cobalt doping rates and furthermore gave upgraded outcome contrasted with honorable metal and rGO-based MoS_2 nanocomposites. Moreover, promptly dispersible in polar solvents like water or methanol, the 6% Co-doped MoS_2 nanosheets exhibited exceptional reactant movement toward decrease of destructive nitrophenol from squander waters at encompassing temperature showing high turnover recurrence (4.18×10^{18} particles per g pers). Furthermore, high bad zeta potential was likewise recognized showing that the so shaped examples are steady against accumulation in scattering medium. Results showed some conceivable clarification for the unrivaled catalyst action of the greatest 6% Co doped MoS_2 layers as it could be because of a blend of (a) adjustment of the metallic 1T stage with expanding electrical conductivity (decline in band hole and enactment energy) and (b) better electron catch from the hydride and electron supply to the nitrophenol substrates through reversible redox responses at the Co locales. Ethiraj et al. (2020) disclosed the degradation of phenolic compounds in the presence of pure and Cu doped nickel oxide (Cu–NiO) nano-catalysts. A wet chemical method was opted for the catalyst preparation. Characterization like fourier transform infrared spectroscopy (FTIR) confirms the formation of pure NiO and the existence of copper in doped nano-catalyst samples. Cu–NiO nano-catalysts samples showed a depletion in average crystallite size as compared to pure NiO sample, where it was 24.0, 22.8, and 19.03 nm for 2Cu–NiO and 4Cu–NiO, respectively. Using TEM, the average particle size as determined were about 28.0, 26.6, and 22.8 nm for NiO, 2Cu–NiO, and 4Cu–NiO, respectively with the energy band gap values of 3.26, 3.64, and 3.87 eV for undoped NiO, 2Cu–NiO and 4Cu NiO respectively. It was also found that under UV radiation for 180 min, 4Cu–NiO nano-catalysts showed

degradation efficiency of 66.36 and 47.00% for 0.3 and 0.4 mol/L, respectively. After 300 min. of UV radiation, the maximum degradation efficiency was 66.83% in 0.3 mol/L (4Cu–NiO), 75.20 and 72.04% was noted in 0.4 and 0.5 mol/L (2Cu–NiO). The maximum amount of phenol (75.2%) was removed at 300 min. Furthermore, photocatalytic performance of Cu–NiO and pure NiO was systematically examined at various reaction times and Cu doping ratios (2–4 wt.%). Different molar concentrations of phenol were taken into consideration for this experiment. The obtained results showed that the Cu–NiO nano-catalyst exhibited the highest phenol degradation efficiency as compared to their undoped composition. Promising results shows the practical application of these materials can be in efficient removal of phenol from real industrial effluent. The nano-catalyst efficiency for phenol removal was tested in real leather industrial wastewater effluent which could remove about 85.7% within 150 min.

You et al. (2010) presented Ag+ doping TiO_2 nanofibers arranged by in-situ and drenching strategies assigned as SI-TiO_2 and IM TiO_2 nanofibers, separately. The creator attempted to assess the impacts of the two different doping techniques on the material properties. The outcomes showed that the two sorts of nanofibers with the breadth of around 20 nm are micron-sized length, and were covered by nano-wads of Ag_2O with the measurement of 2–5 nm. As compared to IM TiO_2 nanofibers, the SI TiO_2 nanofibers have less Ag_2O particles. Along these lines, the photo reactant movement of IM-TiO_2 nanofibers is higher than SI-TiO_2 nanofibers, which is additionally demonstrated in photo catalysis explore showing the debasement proportion of IM-TiO_2 impetus is 100%, and the corruption proportion of SI-TiO_2 impetus is 95%. To further assess the photo catalyst action of IM-TiO_2 and SI-TiO_2 nanofibers, the decay of MB color in arrangement has been analyzed utilizing the IM-TiO_2 and SI-TiO_2 nanofibers under bright light illumination. Preceding light, the MB arrangement over the impetus is for the most part kept in obscurity for 30 min to acquire the harmony adsorption state. It was observed that the corruption of the MB arrangement was done after 200 min when IM-TiO_2 nanofibers were utilized as the impetus. In a similar photo catalysis condition, the debasement proportion of the MB arrangement was just 95% when SI-TiO_2 nanofibers were utilized as the impetus. The corruption proportion of two nanofibers was higher than that of P_{25} (Degussa TiO_2 nanocrystals with 25 nm measurement). For IM-TiO_2 nanofibers, Ag_2O particles were adsorbed on the outer layer of the TiO_2 nanofibers. By and large, on engrossing a photon, an Ag_2O molecule produces an electron and an opening, and consequently the photo created electron consolidates with an Ag+ particle to frame an Ag iota. The adsorptive O_2 on IM-TiO_2 nanofibers go about as electron acceptors to catch photo generated electrons and diminishes the recombination of electrons and openings, as depicted by the accompanying conditions: e– + O_2 = O_2–and Ag++e–=Ag. Under a similar photo catalysis condition, IM-TiO_2 nanofibers and SI-TiO_2 nanofibers were reused as photo impetuses. The corruption proportion of IM-TiO_2 nanofibers and SI-TiO_2 nanofibers after 3 reuses for the MB arrangement was 100 and 95% individually, and the photo catalysis time was 200 min. The two nanofibers showed magnificent soundness for its reuse, 90% of starting movement actually stayed after 5 cycle uses. In the wake of rehashing multiple times, the corruption proportion of IM-TiO_2 nanofibers

and SI-TiO_2 nanofibers was 85.1% and 84.3% individually. Consequently, IM-TiO_2 nanofibers and SI-TiO_2 nanofibers have high photcatalytic activity action and are not difficult to be reused.

Senthilraja et al. (2014) reported the Ag loaded Au–ZnO synthesized by the precipitation–decomposition method. The formed catalyst was characterized by various sophisticated tools like X-Ray Diffraction (XRD), Field Emission Scanning Electron Microscopy (FE-SEM), Energy Dispersive Spectrum (EDS), Transmission Electron Microscopy (TEM), Diffuse Reflectance Spectra (DRS), Photoluminescence spectra (PL) and BET surface area measurements. The photocatalytic activity of Ag–Au–ZnO was investigated for the degradation of Methylene Blue (MB) in aqueous solution using UV-A light. Interestingly, Ag–Au–ZnO was found to be more effective than Ag–ZnO, Au–ZnO, commercial ZnO, bare ZnO, TiO_2-P_25 and TiO_2 (Aldrich) at pH 7 for the mineralization of Methylene Blue dye. The effects of operational parameters such as the amount of photocatalyst, dye concentration, initial pH on photo mineralization of MB dye was examined. The mineralization of MB was confirmed by Chemical Oxygen Demand (COD) measurements. Additionally, a mechanism was proposed for the degradation of MB under UV-A light. A mechanistic scheme of the charge separation and photocatalytic reaction of Ag–Au–ZnO photocatalyst is shown in Scheme 1 (Fig. 4.14).

For the most part, when metal oxide semiconductors (ZnO) are generally uncovered to UV excitation, the delivered electrons/openings induce a response with appended particles on the material surface and produce receptive revolutionaries. The electrons in the conduction band respond with O_2 to frame superoxide anion revolutionaries (O_2 d–) and the openings in the valence band respond with water

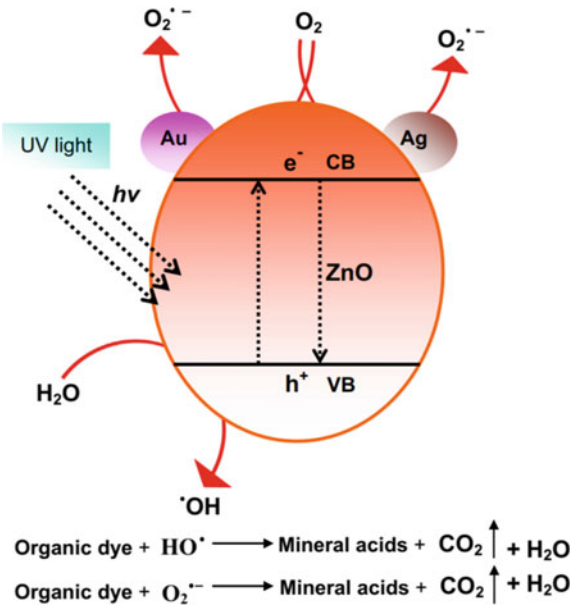

Fig. 4.14 Mechanism of degradation of MB by Ag–Au–ZnO [Reproduced with permissions from Senthilraja et al. (2014)]

to form hydroxyl extremists (dOH) (Lin et al. 2005). Such enacted extremists play the role in degrading the contaminations. It is for the most part proposed that the rate-restricting strides of the photocatalytic response of semiconductors are electron-opening recombination and electron transfer from the ZnO surface to the adsorbed oxygen molecules (Szabó-Bárdos et al. 2003; Goto et al. 2004). "Ag" can trap the electron from conduction band (CB) of the semiconductor to diminish the electron-hole recombination (Subash et al. 2013). "Au" likewise can store the produced electrons by photoexcited electron-opening partition, actuating the Fermi level shift toward more regrettable possibilities. The transfer of electrons to Au go on until the Fermi level approaches the conduction band edge of the semiconductor (Subramanian et al. 2003). Hence Ag and Au enjoy great benefit on moving the photoelectron. Subsequently, the recombination of photoelectron and hole is avoided and the photoinduced age of electron-holepairs will proceed. The diminished electron-opening recombination increases the photocatalytic movement of the impetuses. The superoxide radical anion and hydroxyl revolutionary delivered are used for the corruption of color.

Zhao et al. (2019) reported a progression of Al_2O_3 upheld Cr-doped ZnS semiconductor impetuses with different Cr/Zn molar proportions ready by co-impregnation strategy, and explored in non-warm plasma initiated H_2S disintegration. The as synthesized impetuses were portrayed utilizing XRD, N_2 adsorption/desorption, UV-noticeable spectroscopy, TEM, Raman, ICP and XPS methods. Cr-doped ZnS with various measure of Cr had the essentially upgraded reactant execution, contrasted with undoped ZnS. Varieties in catalyst movement were examined as far as adjustment on the synthetic and actual properties of the Cr-doped ZnS impetuses. Among every one of the impetuses, the Cr0.20–ZnS impetus showed the best reactant conduct with full H_2S transformation at least energy cost. Besides, the drawn out study shows that Cr doped ZnS displays great dependability in H_2S disintegration.

The reactant exhibitions of the different Cr_x–ZnS impetuses were evaluated through H_2S decomposition in non-warm plasma. For comparison, the exhibitions of undoped ZnS and Al_2O_3 support were additionally performed. For the instance of Al_2O_3 support, it might influence both the dispersion of plasma-created dynamic species and the release attributes. On the one hand, Al_2O_3 support has a solid adsorption limit with regards to plasma-produced dynamic species. The adsorption by Al_2O_3 support can drag out the home season of these species. The permeable materials in the hole upgrade the electric field. Both the improved release and the expanded home time are great for H_2S disintegration. More miniature releases, which brought about the inception of synthetic reactions among H_2S atoms, extremists and electrons, happened for Al_2O_3 filled gap. As found in Fig. 4.15, every one of the Cr_x–ZnS impetuses would do well to exercises of H_2S decay than ZnS impetus and Al_2O_3 support, and the H_2S transformation could reach as high as 100%. Examination of the trial results show that the Cr/Zn molar proportion impacted considerably H_2S conversion.

Interestingly, results showed the catalytic activity first increased and then declined with increasing the Cr content with the energy consumption in the decomposition of H_2S and was strongly dependent on the H_2S conversion levels. Among them, the $Cr_{0.20}$–ZnS catalyst exhibited the best catalytic performance, achieving full H_2S

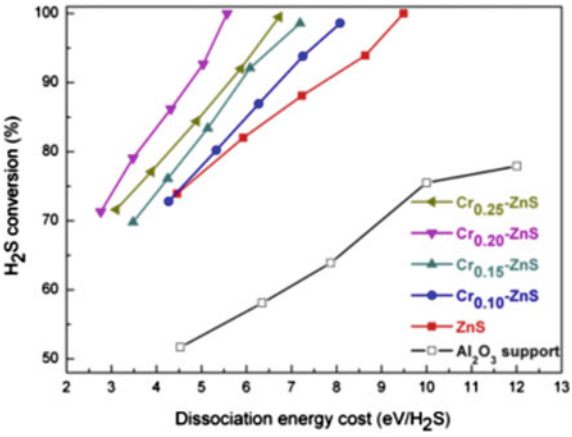

Fig. 4.15 H_2S conversion as a function of dissociation energy cost in the plasma-induced decomposition over the Cr_x–ZnS catalysts with different Cr/Zn molar ratios. Reaction conditions: catalyst bed volume: 15 mL, feed: 20 vol% H_2S in Ar, GHSV: 120 h1 [Reproduced with permissions from Zhao et al. (2019)]

conversion at lowest energy cost. At an energy consumption of 5.57 eV/H_2S, H_2S conversions were 100%, 89.7%, 87.4%, 81.8%, 79.7%, and 55.2% when $Cr_{0.20}$–ZnS, $Cr_{0.25}$–ZnS, $Cr_{0.15}$–ZnS, $Cr_{0.10}$–ZnS, undoped ZnS and Al_2O_3 were filled in the gap, respectively. The characterizations of the Cr_x-ZnS catalysts showed that the chemical and physical properties such as structure, optics, and particle size were dramatically influenced by the Cr/Zn molar ratio. Based on the XRD, TEM, and Raman portrayal, Cr_x–ZnS had the cubic sphalerite structure, and the Cr3+ particles were consistently dispersed in ZnS without isolated debasement stage seen in all the catalysts. Moreover, all the Cr_x–ZnS impetuses showed somewhat high BET surface regions. The reactant exhibitions of the different Cr_x–ZnS catalysts were evaluated through H_2S disintegration in non-warm plasma. Relative exhibitions of undoped ZnS and Al_2O_3 were performed. The high BET surface region is favorable to retain more lights and increment the quantity of the dynamic habitats, as well as shortening the distance for the photo created transporters to come to the surface (Xing et al. 2006; Hu et al. 2005). In the meantime, the molecule size of Cr-doped ZnS was around 8 nm. Little size nanoparticles with unfortunate crystallinity are good for the quick electron transportation from mass to surface, which avoid the recombination of the created electrons and openings in the main part of the catalyst (Bao et al. 2008; Masakazu and Takahit 1987). Along these lines, a reduction in molecule size of Cr doped ZnS likewise added to the higher movement. Fundamentally, the photo physical properties of semiconductor impetus, for example, places of conduction and valence groups and light assimilation, are connected with the synthetic pieces. High reactant exercises of the Cr_x–ZnS impetuses are associated with the low recombination of the openings and electrons and high light assimilation. Moreover, the reasonable debasement energy level could be given through an appropriate doping measure of Cr into the interstitial or cross section of ZnS. This pollutant energy level prompts the simple infusion of the invigorated electrons from valence band (VB) to conduction band (CB) of ZnS (Bodke et al. 2014). The pace of H_2S deterioration over Cr-doped ZnS relies upon the number of inhabitants in opening electron matches. We

revealed that upheld metal sulfide semiconductors (like ZnS/Al_2O_3 and CdS/Al_2O_3) functioned admirably along with DBD plasma in the decay of H_2S (Bao et al. 2008). Metal sulfide semiconductors in the terminal hole can be invigorated by both the solid electric field and light illumination, creating profoundly dynamic opening electron matches. The created opening and electron will respond with the adsorbed surface species, like H_2S, HS, and H+, in this way speeding up the development of H_2 and sulfur (Zhao et al. 2013a, b). In this way, since the created opening electron matches are adequately responsive to change H_2S over completely to H_2 and sulfur, a higher populace of opening electron matches can be connected to the better exhibition on H_2S decay. The progressions in molar proportion of Cr/Zn impacted the photo physical properties of Cr doped ZnS. As portrayed by UV-noticeable spectra (found in Fig. 4.16), with expanding the Cr content, a repetitive variety in the assimilation in apparent light area and band hole of Cr_x–ZnS could be found obviously.

For the impetus with smaller band hole, less energy for electrons is expected to hop from VB to CB. Accordingly, a decline in the band hole of impetus can instigate an

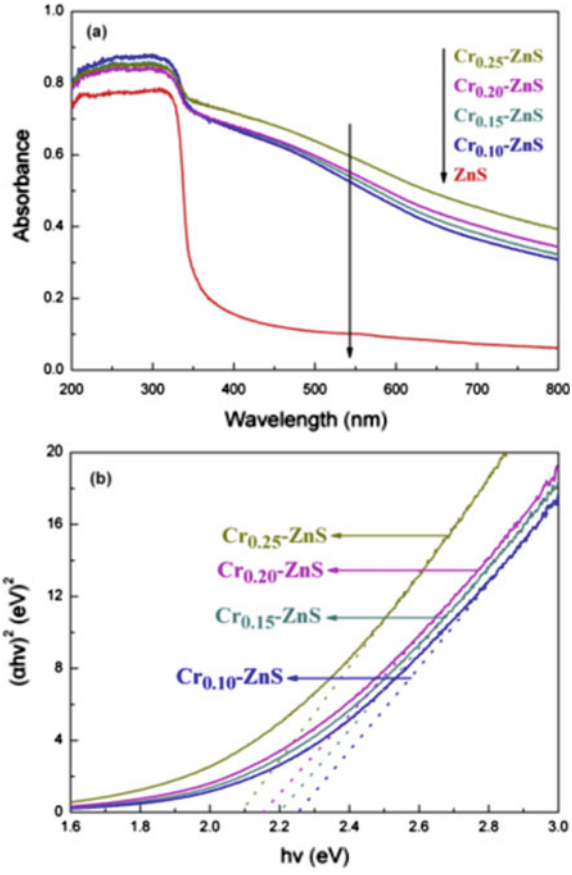

Fig. 4.16 UV-visible diffuse reflection spectra for the ZnS and Cr_x–ZnS catalysts with different Cr/Zn molar ratios [Reproduced with permissions from Zhao et al. (2019)]

increment of opening electron pair populace. Furthermore, the doped Cr3+ particles were approved to be consistently integrated into the interstitial destinations of ZnS grid, which would bring about the outperformed positive charges and the Zn opportunities arrangement. Preferably, one Zn opportunity might be created by the fuse of two Cr3+ particles (Zeng et al. 2012). Subsequently, countless Zn opportunities can be created by the Cr3+ particles consolidation. Zn opportunities advanced the detachment of the energy initiated openings and electrons, which prompted the better catalyst conduct in H_2S deterioration, contrasted and the undoped ZnS impetus. Be that as it may, albeit the $Cr_{0.25}$–ZnS impetus displayed more grounded noticeable light retention than other Cr-doped ZnS impetuses with lower Cr content, the H_2S change was lower. For a diminished catalyst movement of $Cr_{0.25}$ZnS, expanding how much Cr doping would achieve the lopsided dispersion of the Cr3+ particles. The opening electron recombination was considered to become predominant, because of the greater centralization of Cr doping. In this way, a pointless expansion in the Cr content not just given the more recombination habitats to opening electron matches, yet in addition hampered the light assimilation of the Cr-doped ZnS impetuses, hence the catalyst movement was diminished. Creator established that a Cr/Zn molar proportion of 0.20 was the most reasonable for the primary and optical properties regarding H_2S decomposition action. Higher H_2S transformation was gotten for the feed gas with lower H_2S fixation. In the interim, an increment of SIE came about in fundamentally improved H_2S transformation. Reddy et al. (2012a, b) detailed comparable outcomes during the H_2S deterioration in a non-warm plasma. At lower H_2S focus, a bigger piece of the electrons slam into Ar balance gas, demonstrating that Ar balance gas likewise assume fundamental parts in the decay (Zhao et al. 2007). To exhibit the steadiness of the Cr-doped ZnS impetus, $Cr_{0.20}$–ZnS was picked as the delegate impetus to examine the catalyst security at full H_2S conversion and H_2S deterioration response consequence of the $Cr_{0.20}$–ZnS impetus (Fig. 4.17). It uncovered that the reactant action didn't display misfortune in the runs. Besides, the

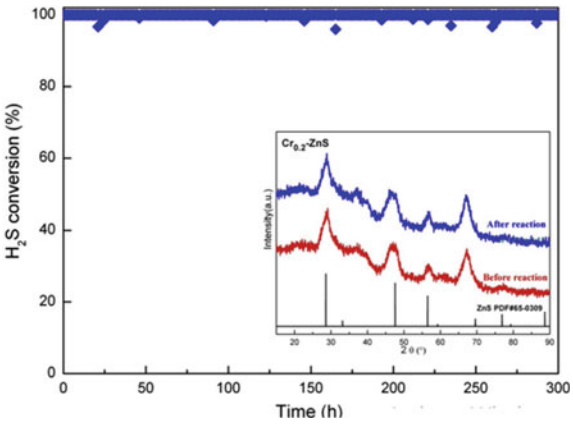

Fig. 4.17 Shows the long-time H_2S decomposition reaction result of the $Cr_{0.20}$–ZnS catalyst [Reproduced with permissions from Zhao et al. (2019)]

XRD profiles of the impetus when the response barely changed demonstrating that the precious stone design went through no variety during the H_2S plasma.

To work on the exhibition of photo electrochemical cells, different metal particles have been integrated into various host semiconductor nanocrystals (Sheng et al. 2020). In any case, such a methodology brings up two new issues that should be paid all due respects to plan and upgrade this new doping technique: (i) how would we precisely assess and rank these dopants? also (ii) how do the dopant related mid hole states tailor the band construction of the host semiconductors and the elements of the photo generated transporters? Creator in this work utilized nanosheet-nanorod ZnO as a detached substrate and CdS as a host for indium, copper, manganese, and cerium doping. Given the uniform actual properties and electronic construction of this climate, the photocurrent thickness and photo electrochemical productivity increment from ZnOeCdS (3.0 mA/cm^2, 0.41%), ZnOeCdSeIn (4.4 mA/cm^2, 0.59%), ZnOeCdSeCu (5.1 mA/cm^2, 0.98%), ZnOeCdSeMn (6.7 mA/cm^2, 1.07%), to ZnOeCdSeCe (8.9 mA/cm^2, 1.9%). With the assistance of electrochemical cyclic voltammetry, open-circuit voltage-rot estimations, and fluorescence spectroscopy, the band edges custom fitted by the mid hole states and the transporter elements not entirely set in stone. Besides, a mind boggling connection between these properties and the material presentation is laid out for precisely interpreting the photo electrochemical action. By observing the OH fixation during light, the powerful photo electrochemical catalyst action is likewise obviously portrayed by involving ZnOeCdSeMn and ZnOCdSeCe as model photocatalysts. Critical work has been done on the photo electrochemical debasement of water-broke down poisons at a lighted semiconductor-electrolyte intersection and plays very much archived the part of hydroxyl revolutionaries (OH). Goodness produced during illumination on the outer layer of a photocatalyst is the fundamental species liable for the corruption of toxin atoms. It is in this manner helpful to screen the convergence of OH to unequivocally assess the catalyst movement (Hisatomi et al. 2014). In this work, the ZnOeCdSeMn and ZnOeCdSeCe photo cathodes are utilized as model photocatalysts. Goodness shaped at these photo cathodes can be distinguished from the photoluminescence strategy utilizing terephthalic corrosive (TA) as a test atom. TA promptly responds with OH to create the emphatically fluorescent item TAOH, and the force of fluorescence is corresponding to how much OH. As displayed in Fig. 4.18a, b, the discharge force increments continuously with expanding light time for both ZnOeCdSeMn and ZnOeCdSeCe. To represent the unique movement of the photocatalysts, the emanation power is gathered each 30 min during illumination. Figure 4.18c shows the relative additions, which demonstrate that the photoelectrochemical catalyst action of ZnOeCdSeCe is better than that of ZnOeCdSeMn. For both model photocatalysts, an enormous grouping of OH shows up during the underlying 90 min of light, trailed by an unmistakable decline in OH fixation. This outcome is predictable with the broadly detailed lessening of the photocatalytic rate, however doesn't totally concur with the clarification given that the contamination beginning focus subordinate rate variety (Sakthivel et al. 2003, p. 2). A seriously convincing clarification is that the impetus deactivation is connected with the photostability. A more cautious investigation of the overall additions in Fig. 18c prompts the end that the photocatalytic movement of ZnOeCdSeCe

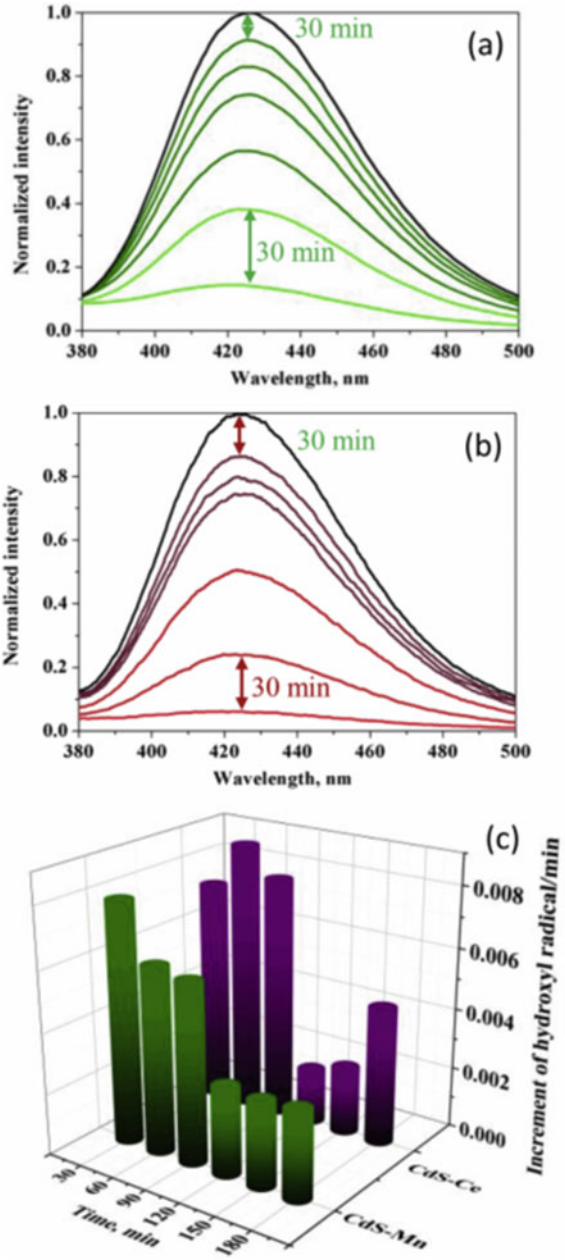

Fig. 4.18 Content change of hydroxyl radical produced on **a** ZnOeCdSeMn, **b** ZnOeCdSeCe under nonstop illumination for 180 min. **c** The variety of the augmentation of the hydroxyl extremist (the information were gathered every 30 min). For instance, the addition rate got at 180 min is the distinction in the standardized photoluminescence power somewhere in the range of 180 and 150 min separated by 30 min [Reproduced with consents from Bryan and Gamelin (2005)]

arrives at the ideal state after 30–60 min of illumination, following which a long downtrend happens that includes an unassuming decrease in photocatalytic action from 60 to 90 min of light, and a strong reduction in photocatalytic action from 90 to 120 min of illumination. Curiously, following this light stage (i.e., the most reduced pace of OH age), a slow increment happens from 120 to 180 min of illumination. For ZnOeCdSeMn, the pace of expansion in OH age step by step diminishes all through the 180 min of illumination.

Note that an unmistakable reduction in the pace of OH age happens from 90 to 120 min of light. After this point, the pace of OH age stays steady. The varieties in the pace of OH age for the two model photocatalysts likewise concur with past reports on long-term photostability tests with photocurrent thickness change (Santra and Kamat 2012; Li et al. 2014; Ertis and Boz 2017) using Ce doped CdS as model impetus showed that photodegradation movement on methyl blue encounters comparable inclination. Ranjith et al. (2018) detailed that debased Rhodamine B utilizing Ni/Ce co-doped CdS NPs as impetuses likewise affirmed a conspicuous expansion in action after 100 min illumination. Xiang et al. (2011) ever precisely and quantitatively concentrated on the OH created on different semiconductor photocatalysts, affirming that the natural properties of semiconductors (counting the band design and stage structure), pH variance impacted the creation paces of OH.

Fu et al. (2020) reported a three-dimensional (3D) photocatalyst synthesized through the self-assembly of graphitic carbon nitride (gC_3N_4), TiO_2, graphene (Gr), and carbon nanotubes (CNTs), in which both Gr and CNTs act as electron mediators, to form an all-solid-state g-C_3N_4/Gr–CNTs/TiO_2 Z-scheme photocatalytic system. In this Z-scheme photocatalyst, the highly interconnected CNTs not only can effectively promote the transfer of photogenerated charge carriers, but also built a 3D open frame network to harvest more incident light and provide more specific surface area for photoreactions. Benefiting from the 3D nanostructure and Z scheme system, phenol removal over g-C_3N_4/GrCNTs/TiO_2 reached up to 90% within 120 min using a high-pressure Xe short-arc lamp as light source, which was much higher than that achieved over pure g-C_3N_4. The 3D Z-scheme photocatalyst fabricated in this study may be an attractive material for many environmental and energy-related applications. The photocatalytic activity of g-C_3N_4/Gr–CNTs/TiO_2 was evaluated using phenol as the substrate. Before light irradiation, the mixed solution of phenol and photocatalyst was stirred for 60 min to attained absorption equilibrium. Approximately 9% of phenol was absorbed by gC_3N_4/Gr–CNTs/TiO_2. Approximately 90% of phenol was removed after light irradiation for 120 min in the presence of 3D CN–Gr–C–T_3, while 50%, 68%, and 81% of phenol was removed using 3D CN–Gr–C–T1, 3D CN–Gr–C–T2, and 3D CN–Gr–C–T4 respectively.

Apparently, there is an optimum Gr–CNTs content in g-C_3N_4/Gr–CNTs/TiO_2. When the mass ratio of g-C_3N_4 to Gr–CNTs is lower than 0.7, the photocatalytic activity of g-C_3N_4/Gr-CNTs/TiO_2 increased gradually as the Gr–CNTs content increased. However, when the Gr-CNTs content was increased further, the photocatalytic activity of g-C_3N_4/Gr–CNTs/TiO_2 decreased; this may be because excess Gr–CNTs hinder the light absorption of photocatalysts. In addition, the pure g-C_3N_4 and pure TiO_2 exhibits a lower phenol removal rate than that of 3D g-C_3N_4/GrCNTs/TiO_2

photocatalysts. In order to reveal the reactive oxygen species, the ESR spin-trapping technique has been applied using DMPO as the spin-trap reagent (Chen et al. 2018, 2019). The typical quartet peaks with a 1:2:2:1 intensity are observed for g-C_3N_4/Gr–CNTs/TiO_2 under irradiation, which could be ascribed to the DMPO-%OH adduct derived from H_2O oxidization by photogenerated holes (Huang et al. 2017). Meanwhile, it can be seen from Fig. 18b that evident six identical peaks appeared, which is assigned to DMPO-%O^{2-} adduct derived from O^2 reduction by photogenerated electrons (Li et al. 2020), whereas no ESR signals were observed in the dark. This result indicated that both hydroxyl radicals (%OH) and superoxide anion radicals (%O^{2-}) are the dominant reactive radicals in photocatalytic process.

Previous works have confirmed that both g-C_3N_4 and TiO_2 are suitable candidates to construct the Z-scheme photocatalyst because of their matched band gap positions and extremely strong anti-light corrosion (Lu et al. 2018; Wang and Liu 2019).

When the g-C_3N_4/Gr CNTs/TiO_2 is irradiated with incident light, a typical Z-scheme system is formed with g-C_3N_4, TiO_2, Gr and CNTs. In this artificial Z-scheme system, g-C_3N_4 and TiO_2 serve as the PS I and PS II, respectively. When the incident light energy is larger than the energy gap of g-C_3N_4 and TiO_2, the photogenerated electrons in the valence band (VB) would be migrated to the conduction band (CB) and left photogenerated holes in the VB. Particularly, benefiting from the super conductivity, CNTs could be served as the solid-state electron mediators and provide pathways for the photogenerated electrons in TiO_2 and the photogenerated holes in g-C_3N_4 moving to the Gr and following to recombine in the Gr. Meanwhile, the photogenerated electrons in the CB of g-C_3N_4 accumulate to form an electron rich region and the photogenerated holes in the VB of TiO_2 accumulate to form a hole-rich region. Obviously, the electrons in the CB of g-C_3N_4 could reduce O_2 to yield superoxide anion radicals (%O^{2-}), and the holes in the VB of TiO_2 could oxidize H_2O to yield hydroxyl radicals (%OH). Therefore, this artificial Z-scheme g-C_3N_4/Gr–CNTs/TiO_2 features the spatial isolation of photogenerated electrons and holes, resulting in the efficient charge separation and enhanced photocatalytic activities.

4.4 Conclusion

In modern era, researchers have developed that the semiconductors after doping of impurities could impact various catalytic, electrical, optical and magnetic properties of the materials. Deep studies have been performed all around the universe on atoms such as Mn, Cu, Co, and many other doped semiconductor materials for their novel advanced properties and their application in diverse fields. Semiconductors with magnetic impurities, also known as diluted magnetic semiconductors or semi-magnetic semiconductors, have been explored for decades.

This chapter has been an extensive review for classification of existing photocatalytic materials and the methods for development of their performance as catalysts. The potential industrial application usage of this technology is also discussed in detail.

References

Ahmad M, Ahmed E, Ahmed W, Elhissi A, Hong ZL, Khalid NR (2014) Enhancing visible light responsive photocatalytic activity by decorating Mn-doped ZnO nanoparticles on graphene. Ceram Int 40(7):10085–10097

Ali T, Ahmed A, Alam U, Uddin I, Tripathi P, Muneer M (2018) Enhanced photocatalytic and antibacterial activities of Ag-doped TiO_2 nanoparticles under visible light. Mater Chem Phys 212:325–335

Ambigadevi J, Kumar PS, Vo D-VN, Haran SH, Raghavan TS (2020) Recent developments in photocatalytic remediation of textile effluent using semiconductor based nanostructured catalyst: a review. J Environ Chem Eng, p 104881

Bao N, Shen L, Takata T, Domen K (2008) Self-templated synthesis of nanoporous CdS nanostructures for highly efficient photocatalytic hydrogen production under visible light. Chem Mater 20(1):110–117

Bi X et al (2020) Construction of g-C_3N_4/TiO_2 nanotube arrays Z-scheme heterojunction to improve visible light catalytic activity. Colloids Surf, A 603:125193

Bodke MR, Purushotham Y, Dole BN (2014) Crystallographic and optical studies on Cr doped ZnS nanocrystals. Cerâmica 60(355):425–428

Bryan JD, Gamelin DR (2005) Doped semiconductor nanocrystals: synthesis, characterization, physical properties, and applications. Prog Inorg Chem 54(47):47–126

Chen S, Pan Y (2021) Noble metal interlayer-doping enhances the catalytic activity of 2H–MoS_2 from first-principles investigations. Int J Hydrogen Energy 46(40):21040–21049

Chen F et al (2018) Thickness-dependent facet junction control of layered $BiOIO_3$ single crystals for highly efficient CO_2 photoreduction. Adv Func Mater 28(46):1804284

Chen F, Huang H, Guo L, Zhang Y, Ma T (2019) The role of polarization in photocatalysis. Angew Chem Int Ed 58(30):10061–10073

Chen C et al (2020) Synthesis of a flower-like SnO/ZnO nanostructure with high catalytic activity and stability under natural sunlight. J Alloy Compd 826:154122

Dave S, Khan AM, Purohit SD, Suthar DL (2021a) application of green synthesized metal nanoparticles in the photocatalytic degradation of dyes and its mathematical modelling using the caputo–fabrizio fractional derivative without the singular kernel. J Math. https://doi.org/10.1155/2021/9948422

Dave S, Jagtap P, Verma S, Nehra R, Dave S, Mohanty P, Das J (2021b) Mathematical modeling and surface response curves for green synthesized nanomaterials and their application in dye degradation. Photocat Degrad Dyes 1:571–591

Dave S, Dave S, Das J (2021c) Photocatalytic degradation of dyes in textile effluent: a green approach to eradicate environmental pollution. In: The future of effluent treatment plants. Elsevier, pp 199–214

Demirci S, Dikici T, Yurddaskal M, Gultekin S, Toparli M, Celik E (2016) Synthesis and characterization of Ag doped TiO_2 heterojunction films and their photocatalytic performances. Appl Surf Sci 390:591–601

Ertis IF, Boz I (2017) Synthesis and characterization of metal-doped (Ni Co, Ce, Sb) CdS catalysts and their use in methylene blue degradation under visible light irradiation. Modern Res Catal 6(01):1

Ethiraj AS, Uttam P, Varunkumar K, Chong KF, Ali GA (2020) Photocatalytic performance of a novel semiconductor nanocatalyst: copper doped nickel oxide for phenol degradation. Mater Chem Phys 242:122520

Fu Z, Wang H, Wang Y, Wang S, Li Z, Sun Q (2020) Construction of three-dimensional g-C_3N_4/Gr-CNTs/TiO_2 Z-scheme catalyst with enhanced photocatalytic activity. Appl Surf Sci 510:145494

Giahi M, Pathania D, Agarwal S, Ali GA, Chong KF, Gupta VK (2019) Preparation of Mg-doped TiO_2 nanoparticles for photocatalytic degradation of some organic pollutants. Studia UBB Chemia 64:7–18

González-Rodríguez J et al (2020) Enhanced photocatalytic activity of semiconductor nanocomposites doped with ag nanoclusters under UV and visible light. Catalysts 10(1):31

Goto H, Hanada Y, Ohno T, Matsumura M (2004) Quantitative analysis of superoxide ion and hydrogen peroxide produced from molecular oxygen on photoirradiated TiO_2 particles. J Catal 225(1):223–229

Guha S et al (2003) Temperature-dependent optical studies of $Ti_{1-x}Co_xO_2$. Appl Phys Lett 83(16):3296–3298

Guillén-Santiago A, Mayén SA, Torres-Delgado G, Castanedo-Pérez R, Maldonado A, de la L. Olvera M (2010) Photocatalytic degradation of methylene blue using undoped and Ag-doped TiO_2 thin films deposited by a sol-gel process: effect of the ageing time of the starting solution and the film thickness. Mater Sci Eng B 174(1–3):84–87

Hisatomi T, Kubota J, Domen K (2014) Recent advances in semiconductors for photocatalytic and photoelectrochemical water splitting. Chem Soc Rev 43(22):7520–7535

Houas A, Lachheb H, Ksibi M, Elaloui E, Guillard C, Herrmann J-M (2001) Photocatalytic degradation pathway of methylene blue in water. Appl Catal B 31(2):145–157

Hu J-S et al (2005) Mass production and high photocatalytic activity of ZnS nanoporous nanoparticles. Angew Chem Int Ed 44(8):1269–1273

Huang H, Tu S, Zeng C, Zhang T, Reshak AH, Zhang Y (2017) Macroscopic polarization enhancement promoting photo-and piezoelectric-induced charge separation and molecular oxygen activation. Angew Chem Int Ed 56(39):11860–11864

Ilkme ES, Soylu GSP (2021) The role of some metal ions in enhancement of photocatalytic activity of Fe_2O_3-V_2O_5 binary oxide. Turk J Chem 45(2):348–361

Khlyustova A, Sirotkin N, Kusova T, Kraev A, Titov V, Agafonov A (2020) Doped TiO_2: the effect of doping elements on photocatalytic activity. Mater Adv 1(5):1193–1201

Khurshid F, Jeyavelan M, Hudson MSL, Nagarajan S (2019) Ag-doped ZnO nanorods embedded reduced graphene oxide nanocomposite for photo-electrochemical applications. R Soc Open Sci 6(2):181764

Kumar R, Rana D, Umar A, Sharma P, Chauhan S, Chauhan MS (2015) Ag-doped ZnO nanoellipsoids: potential scaffold for photocatalytic and sensing applications. Talanta 137:204–213

Kwon YT, Song KY, Lee WI, Choi GJ, Do YR (2000) Photocatalytic behavior of WO_3-loaded TiO_2 in an oxidation reaction. J Catal 191(1):192–199

Lachheb H et al (2002) Photocatalytic degradation of various types of dyes (Alizarin S, Crocein Orange G, Methyl Red, Congo Red, Methylene Blue) in water by UV-irradiated titania. Appl Catal B 39(1):75–90

Lee H et al (2018) Comparative study of catalytic activities among transition metal-doped IrO_2 nanoparticles. Sci Rep 8(1):1–8

Li D, Haneda H, Ohashi N, Hishita S, Yoshikawa Y (2004) Synthesis of nanosized nitrogen-containing MO_x–ZnO(M=W, V, Fe) composite powders by spray pyrolysis and their visible-light-driven photocatalysis in gas-phase acetaldehyde decomposition. Catal Today 93:895–901

Li W et al (2014) Stable core/shell CdTe/Mn-CdS quantum dots sensitized three-dimensional, macroporous ZnO nanosheet photoelectrode and their photoelectrochemical properties. ACS Appl Mater Interfaces 6(15):12353–12362

Li J et al (2020) Unraveling the mechanism of binary channel reactions in photocatalytic formaldehyde decomposition for promoted mineralization. Appl Catal B 260:118130

Li K et al (2021) New insight into the mechanism of enhanced photo-Fenton reaction efficiency for Fe-doped semiconductors: A case study of Fe/g-C_3N_4. Catal Today 371:58–63

Lin H-F, Liao S-C, Hung S-W (2005) The dc thermal plasma synthesis of ZnO nanoparticles for visible-light photocatalyst. J Photochem Photobiol, A 174(1):82–87

Liu G-S et al (2018) In situ electrospinning iodine-based fibrous meshes for antibacterial wound dressing. Nanoscale Res Lett 13(1):1–7

Lu L, Wang G, Zou M, Wang J, Li J (2018) Effects of calcining temperature on formation of hierarchical TiO_2/g-C_3N_4 hybrids as an effective Z-scheme heterojunction photocatalyst. Appl Surf Sci 441:1012–1023

Masakazu A, Takahit S (1987) Photocatalytic hydrogenation of CH_3CCH with H_2O on small-particle TiO_2: size quantization effects and reaction intermediates. Chem 91:4305–4310

Moballegh A, Shahverdi HR, Aghababazadeh R, Mirhabibi AR (2007) ZnO nanoparticles obtained by mechanochemical technique and the optical properties. Surf Sci 601(13):2850–2854

Mohammed MK (2020) Sol-gel synthesis of Au-doped TiO_2 supported SWCNT nanohybrid with visible-light-driven photocatalytic for high degradation performance toward methylene blue dye. Optik 223:165607

Muñoz-Fernandez L, Sierra-Fernández A, Milošević O, Rabanal ME (2016) Solvothermal synthesis of Ag/ZnO and Pt/ZnO nanocomposites and comparison of their photocatalytic behaviors on dyes degradation. Adv Powder Technol 27(3):983–993

Nigussie GY et al (2018) Antibacterial activity of Ag-doped TiO_2 and Ag-doped ZnO nanoparticles. Int J Photoenergy 2018

Rahman MA (2014) A review on semiconductors including applications and temperature effects in semiconductors. Am Sci Res J Eng Technol Sci (ASRJETS) 7(1):50–70

Rahman R, Samanta D, Pathak A, Nath TK (2021) Tuning of structural and optical properties with enhanced catalytic activity in chemically synthesized Co-doped MoS_2 nanosheets. RSC Adv 11(3):1303–1319

Ranjith R, Krishnakumar V, Boobas S, Venkatesan J, Jayaprakash J (2018) An efficient photocatalytic and antibacterial performance of Ni/Ce–Codoped CdS nanostructure under visible light irradiation. ChemistrySelect 3(32):9259–9267

Reddy EL, Biju VM, Subrahmanyam C (2012a) Production of hydrogen from hydrogen sulfide assisted by dielectric barrier discharge. Int J Hydrogen Energy 37(3):2204–2209

Reddy EL, Biju VM, Subrahmanyam C (2012b) Production of hydrogen and sulfur from hydrogen sulfide assisted by nonthermal plasma. Appl Energy 95:87–92

Sakthivel S, Neppolian B, Shankar MV, Arabindoo B, Palanichamy M, Murugesan V (2003) Solar photocatalytic degradation of azo dye: comparison of photocatalytic efficiency of ZnO and TiO_2. Sol Energy Mater Sol Cells 77(1):65–82

Santra PK, Kamat PV (2012) Mn-doped quantum dot sensitized solar cells: a strategy to boost efficiency over 5%. J Am Chem Soc 134(5):2508–2511

Satapathy S, Acharya D, Dixit PK, Mishra G, Das J, Dave S (2021) Mechanistic aspects and rate-limiting steps in green synthesis of metal and metal oxide nanoparticles and their potential in photocatalytic degradation of textile dye. In: Photocatalytic degradation of dyes. Elsevier, pp 605–630

Senthilraja A, Subash B, Krishnakumar B, Rajamanickam D, Swaminathan M, Shanthi M (2014) Synthesis, characterization and catalytic activity of co-doped Ag–Au–ZnO for MB dye degradation under UV-A light. Mater Sci Semicond Process 22:83–91

Shah M, Dave S, Das J (2021) Photocatalytic degradation of dyes current trends and future perspectives

Sheng P et al (2020) The origin of enhanced photoelectrochemical activity in metal-ion-doped ZnO/CdS quantum dots. J Alloy Compd 822:153700

Subash B, Krishnakumar B, Pandiyan V, Swaminathan M, Shanthi M (2013) Synthesis and characterization of novel WO_3 loaded Ag–ZnO and its photocatalytic activity. Mater Res Bull 48(1):63–69

Subramanian V, Wolf EE, Kamat PV (2003) Green emission to probe photoinduced charging events in ZnO−Au nanoparticles. Charge distribution and Fermi-level equilibration. J Phys Chem B 107(30):7479–7485

Szabó-Bárdos E, Czili H, Horváth A (2003) Photocatalytic oxidation of oxalic acid enhanced by silver deposition on a TiO_2 surface. J Photochem Photobiol, A 154(2–3):195–201

Tong H, Ouyang S, Bi Y, Umezawa N, Oshikiri M, Ye J (2012) Nano-photocatalytic materials: possibilities and challenges. Adv Mater 24(2):229–251

Vallejo W, Cantillo A, Díaz-Uribe C (2020) Methylene blue photodegradation under visible irradiation on Ag-Doped ZnO thin films. Int J Photoenergy 2020

Wang X, Liu M (2019) Photocatalytic enhancement mechanism of direct Z-scheme heterojunction Og-C_3N_4@ Fe-TiO_2 under visible-light irradiation. Appl Surf Sci 485:353–360

Xiang Q, Yu J, Wong PK (2011) Quantitative characterization of hydroxyl radicals produced by various photocatalysts. J Colloid Interface Sci 357(1):163–167

Xing C, Zhang Y, Yan W, Guo L (2006) Band structure-controlled solid solution of $Cd_{1-x}Zn_xS$ photocatalyst for hydrogen production by water splitting. Int J Hydrogen Energy 31(14):2018–2024

Yang S, Lee H (2017) Determining the catalytic activity of transition metal-doped TiO_2 nanoparticles using surface spectroscopic analysis. Nanoscale Res Lett 12(1):1–8

You Y, Wan L, Zhang S, Xu D (2010) Effect of different doping methods on microstructure and photo-catalytic activity of Ag_2O–TiO_2 nanofibers. Mater Res Bull 45(12):1850–1854

Zeng X, Zhang J, Huang F (2012) Optical and magnetic properties of Cr-doped ZnS nanocrystallites. J Appl Phys 111(12):123525

Zhang F et al (2019) Recent advances and applications of semiconductor photocatalytic technology. Appl Sci 9(12):2489

Zhao G-B et al (2007) Production of hydrogen and sulfur from hydrogen sulfide in a nonthermal-plasma pulsed corona discharge reactor. Chem Eng Sci 62(8):2216–2227

Zhao L et al (2013a) Decomposition of hydrogen sulfide in non-thermal plasma aided by supported CdS and ZnS semiconductors. Green Chem 15(6):1509–1513

Zhao L, Wang Y, Li X, Wang A, Song C, Hu Y (2013b) Hydrogen production via decomposition of hydrogen sulfide by synergy of non-thermal plasma and semiconductor catalysis. Int J Hydrogen Energy 38(34):14415–14423

Zhao L, Wang Y, Wang A, Li X, Song C, Hu Y (2019) Cr–doped ZnS semiconductor catalyst with high catalytic activity for hydrogen production from hydrogen sulfide in non-thermal plasma. Catal Today 337:83–89

Zhong JB et al (2012) Improved photocatalytic performance of Pd-doped ZnO. Curr Appl Phys 12(3):998–1001